lubricants

MDPI

Article

Experimental Identification of the Void Fraction in a Large Hydrodynamic Offset Halves Bearing

Alexander Engels [1,*], Sören Wettmarshausen [2], Michael Stottrop [1], Thomas Hagemann [2], Christoph Weißbacher [3], Hubert Schwarze [2] and Beate Bender [1]

[1] Product Development, Ruhr-University Bochum, 44801 Bochum, Germany; michael.stottrop@ruhr-uni-bochum.de (M.S.); bender@lpe.ruhr-uni-bochum.de (B.B.)
[2] Institute of Tribology and Energy Conversion Machinery, Clausthal University of Technology, 38678 Clausthal-Zellerfeld, Germany; wettmarshausen@itr.tu-clausthal.de (S.W.); hagemann@itr.tu-clausthal.de (T.H.); schwarze@itr.tu-clausthal.de (H.S.)
[3] Gleitlagertechnik Weißbacher GmbH, 46519 Alpen, Germany; cweissbacher@gtwalpen.de
* Correspondence: alexander.engels@ruhr-uni-bochum.de

Abstract: A common approach to optimising hydrodynamic journal bearings for power loss is to reduce the lubricant supply and direct the oil to specific bearing areas where it is needed to guarantee safe operation. This requires information on the processes in the gap and the surrounding pocket areas for both pre-design and simulation. In this paper, a system consisting of a total of eight cameras is used to determine the void fraction in deep grooves outside the lubricant film. The void fraction in the lubrication gap is determined using a novel method for the evaluation of two proximity measurements. While the variation of the deep groove void fraction is realised by a special oil supply and radially adjustable deep groove elements, the gap void fraction is adjusted by the oil supply in the lube oil pockets at the pad leading edges. On the one hand, the experimental investigations show that the void fraction of the deep groove areas has hardly any influence on the general operating behaviour. On the other hand, the void fraction in the lubrication gap can be measured quantitatively for the first time, and the operating point-dependent gas fractions can be visualised. It is also shown that gaseous cavitation is the main mechanism in partially filled regions of the lubrication gap.

Keywords: large hydrodynamic journal bearings; turbomachinery applications; power loss; operational safety; bearing efficiency; void fraction; density ratio; fractional film content; gaseous cavitation; test rig; distance measurement

check for updates

Received: 9 December 2024
Revised: 22 December 2024
Accepted: 27 December 2024
Published: 29 December 2024

Citation: Engels, A.; Wettmarshausen, S.; Stottrop, M.; Hagemann, T.; Weißbacher, C.; Schwarze, H.; Bender, B. Experimental Identification of the Void Fraction in a Large Hydrodynamic Offset Halves Bearing. *Lubricants* **2025**, *13*, 7. https://doi.org/10.3390/lubricants13010007

Copyright: © 2024 by the authors. Licensee MDPI, Basel, Switzerland. This article is an open access article distributed under the terms and conditions of the Creative Commons Attribution (CC BY) license (https://creativecommons.org/licenses/by/4.0/).

1. Introduction

Large hydrodynamic journal bearings are installed in a wide range of turbomachinery applications, such as turbines or general machines for power generation. Due to advancing climate change [1] and the associated need to lower the dissipation of all machine elements involved in the energy conversion process, it is necessary to optimise currently used large hydrodynamic journal bearings in terms of power loss without endangering operational safety [2].

The basis for all optimisation in this field is an improved understanding of the physical processes in the lubrication gap, pocket areas, and space between pads. While the gap areas are characterised by a small distance between the shaft and the bearing surface in the micrometre range, the adjacent deep groove areas have distances of several millimetres. Despite more than a century of intensive research, the interaction between these single

areas, especially in large hydrodynamic journal bearings with high rotational speeds and radial loads, is still not completely understood.

To this day, the basis for describing the processes in the lubrication gap and the general journal bearing behaviour is the Reynolds equation established by Reynolds in 1886 [3]. While this equation is suitable to describe fluid flow and pressure generation in convergent, completely filled gap regions, its classical form provides high tensile stresses in the divergent gap regions [4]. However, despite the fact that the possibility of limited negative pressures, i.e., tensile stresses, in fluids has been known for several years [5], this scenario seems implausible for hydrodynamic journal bearings under significant shear stresses due to high speeds and specific bearing loads [6]. In areas of high gap widths and shear rates, hydrodynamic journal bearings will, at some point, experience a *film rupture* [7], the characteristics of which can be completely different depending on the application and environmental conditions. The main cause of lubricant film rupture is *cavitation*, which is defined as a disruption of a continuous liquid phase [8]. In general, a distinction is made between three different main categories of cavitation:

- *Vapour cavitation*: pressure drops below the vapour pressure of the liquid, causing vapour bubbles to form and collapse under high energy.
- *Gaseous cavitation*: pressure drops cause dissolved gases to come out of solution, forming gas bubbles that interfere with lubrication but collapse with low energy.
- *Pseudo cavitation*: external gases entering the system cause bubbles to form, disrupting lubrication without a pressure-induced phase change.

Regardless of the type of cavitation, as soon as cavitation increases, the result is an increase of the air content, which is usually described by the term *void fraction*. The current understanding of cavitation was founded by Swift [9] and Stieber [10] with the Swift–Stieber boundary condition in the early 1930s. Jacobson and Floberg [11] are the first to fully describe film rupture and reformation. This theory was later expanded by Olsson [12] to become the JFO theory, which is still used today and has been validated multiple times in experiments. Compared with the Reynolds equation, the JFO theory also fulfils the conservation of mass in the cavitation region. Elrod [13] provided the first numerical implementation of JFO theory. He divided the lubrication gap into a full film zone, where Reynolds equation is valid, and a cavitation zone that is described by a transport equation with pure Couette flow. In the 1950s, ref. [14,15] were among the first to experimentally visualise cavitation between a rotating shaft against a transparent plexiglass bearing shell using a special submerged apparatus. Air bubbles in fingerlike shape were reported. With a similar experimental setup, Smith [16] made one of the first representative experimental recordings of film rupture and film reformation through a plexiglass pane in the 1970s. The references [17–19] summarise the experimental and theoretical knowledge gained on cavitation in journal bearings up to this time. Swales [18] differentiates the nature of cavitation into four different types:

- *Travelling* cavitation.
- *Fixed* cavitation.
- *Vortex* cavitation.
- *Vibratory* cavitation.

Here, *travelling*, *fixed*, and *vibratory* cavitation are unstable. The authors show that when cavitation occurs stably, it is usually gaseous cavitation. In 1982, Jacobson, B.O., and Hamrock, B. J., showed gaseous cavitation in their publication [20]. They used a journal bearing with a diameter of 90 mm and a high-speed motion picture camera to capture the cavitation. Later, in 1983, they additionally observed vapour cavitation for the first time [21]. In 1986 [22], Hopf et al. published the first full-scale, high-resolution experimental results of

a 500 mm lemon bore turbine bearing. The capacitively measured lubricant film thickness curves from the shaft indicated film rupture areas at the pad leading and trailing edges. Sun and Brewe [23] carry out experiments on cavitation identification using a camera system on radial journal bearings with diameters of 85 mm and rotational speeds of 1000 min^{-1}. They identify vapour cavitation due to different measured whirling orbits and frequency spectra. In 2010, Braun and Hannon [6] provided a comprehensive overview of the experimental and simulative status of experimental and analytical research on cavitation in journal bearings up to this time. Their analysis revealed significant inconsistencies in the experimental findings, particularly with regard to the bearing areas in which cavitation occurs and the nature of cavitation itself. Shen et al. [24] conducted experiments with a textured axial plain bearing in 2013. They find that gaseous cavitation can occur at pressures of up to 0.3 bar. Many authors also refer to *bubbling oil*, which, unlike cavitation, where air cavities are formed due to a drop in fluid pressure below the saturation vapour pressure, already contains bubbling air when it is injected. Bubbly oil and pseudo cavitation are closely related. In 2014, Yang et al. [25] experimentally investigated "bubbly", respectively oil, at different shear rates and temperatures using a special test rig. The results of their investigations show that the effective viscosity decreases at high shear rates and increases at lower shear rates. Poddar and Tandon [26] built an experimental setup to detect vapour cavitation in a small journal bearing with an acoustic emission sensor. They also use a transparent bearing and a camera to optically detect vapour cavitation. Ochiai et al. [27] investigate the void fraction in a small hydrodynamic journal bearing with low circumferential speed and load. They optically detect areas of gaseous cavitation in the divergent areas of the loaded pad and at the axial edges of the upper, unloaded pad, particularly under starved lubrication. In 2022, Hagemann et al. [28] investigated the Offset Halves Bearing also used in this publication with regard to the effects of the power loss-reducing design on operational safety and power loss. Cavitation areas are revealed in the rapidly diverging gap areas, which up to this point could only be recorded qualitatively. With the same setup, ref. [29] capacitively detected partial fillings can be seen on the unloaded pads of a non-flooded large radial tilting pad bearing. In a later comparison with the same bearing as a flooded version, first published in [30], Stottrop et al. [31] also show large, partially filled areas on the unloaded pads as well as at the leading and trailing edges of the loaded pads. Comparable results also can be seen when the same bearing with polymer coating is examined [32]. Reinke et al. used a special test rig to investigate various cavitation phenomena [33]. The apparatus simulates a hydrodynamic journal bearing with a diameter of 150 mm and a width of 111 mm, which lies on the end face. Circumferential speeds of about 3.4 m/s and a minimum lubricant film thickness of 173 µm are reached. In [34], bubble generation and transportation were initially investigated. Later investigations used high-speed cameras to optically demonstrate both gaseous cavitation [35] and vapour cavitation [36].

Most of the sources listed investigate vapour, fewer gaseous cavitation in hydrodynamic journal bearings. In these studies, the most common method is optical detection by using cameras. As early as 1953, Rosenberg [37] realised that in various experiments in which cavitation was detected optically in this way, the types of cavitation were mistakenly confused. Recent studies analyse vapour cavitation with acoustic emission sensors. The bearing diameter and the circumferential speeds are, in comparison to large-scale journal bearings for primary energy supply, low in each of the analysed publications. Moreover, the specific bearing load applied is rarely documented. None of the sources analyse the void fraction or cavitation and its influence on general operating behaviour quantitatively. In addition, there is no source that investigates cavitation in hydrodynamic journal bearings with high circumferential speeds and high specific loads experimentally. Most setups

also deliberately provoke cavitation but do not represent a realistic environment of the journal bearing so that it can be analysed in an application-oriented scenario. Thus, there are no known methods to quantitatively determine the void fraction in a realistic and representative experimental setting.

In this context, the following research questions arise regarding the void fraction and the connected phenomenon of cavitation in large hydrodynamic journal bearings:

- What are the differences between the lubrication gap and the deep groove areas, and how do these regions interact with each other?
- In which bearing regions is lubricant present, and where is it absent?
- What is the composition of the lubricant in these regions, or more specifically, what is the oil and air ratio?
- How does the distribution and composition of the lubricant affect the overall operating behaviour?

The aim of this paper is to answer the previously posed research questions by identifying and analysing the *void fraction* in a large hydrodynamic journal bearing. For this purpose, an understanding of the lubricant distribution and composition for subsequent optimisation needs to be gained. Therefore, void fraction generated by varying oil supply and operating conditions is experimentally analysed. Moreover, its impact on operational safety, defined by minimum lubricant film thickness h_{min}, maximum lubricant film temperature T_{max}, and maximum lubricant film pressure p_{max}, as well as the power loss converted by the energy dissipated in the lubricant film P_{fric}, is identified.

2. Materials and Methods

2.1. Power Reduced Offset Halves Bearing

In contrast to bearings of smaller sizes, in large hydrodynamic radial journal bearings, high circumferential speeds, power losses, and thermomechanical deformations can occur. Some effects of smaller-sized bearings can therefore not be scaled to large bearings, which is why an *Offset Halves Bearing* (OHB), shown in Figure 1, is analysed in its original size.

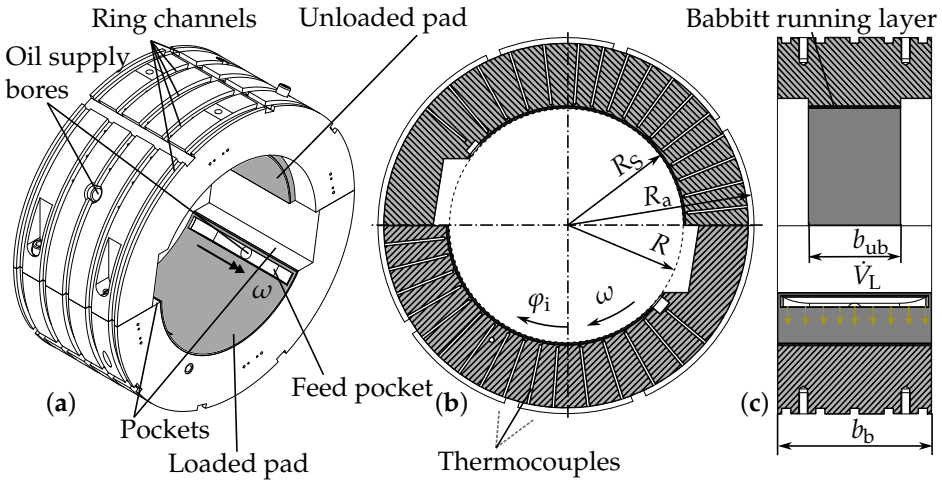


Figure 1. Test bearing design of OHB; (**a**): OHB in isometric view; (**b**): OHB in axial section from drive direction at $b_{\mathrm{b}} = 97.5$ mm; (**c**): OHB in radial section.

A special feature is the improved efficiency design, which includes reduced pad size and two deep grooves between the pads. Detailed information can be found in [28]. The large dimensions and the special design of the bearing allow for the installation of additional measurement technology that would be almost impossible to implement in smaller bearings. An isometric view in Figure 1a shows most of the features described

below. View Figure 1b shows the bearing in axial section from the direction of the drive, i.e., in the direction of ω, at $b_b = 97.5$ mm. In Figure 1c, a radial section shows the wide lube oil pocket of the loaded pad in plan view as well as the unloaded, shortened pad. The detailed geometric parameters are listed in Table 1.

Table 1. OHB parameters.

Parameter	Symbol	Value	Unit
Relative Bearing Clearance	Ψ_i	$1.20^{+0.09}$	10^{-3}
Profiling	Ψ_v	$1.75^{+0.12}_{-0.07}$	1
Inner bearing radius	R	$250.235^{+0.022}$	mm
Radius of the pad	R_S	$250.460^{+0.022}$	mm
Outer bearing radius	R_a	400	mm
Width of the loaded pad	b_b	350	mm
Width of the unloaded pad	b_{ub}	210	mm

When installed, the bearing is rotated under $\varphi_{inst} = -35°$ and positioned axially in the centre of the octagon frame, shown in Figure 2. The ring channels shown in Figure 1 are distributed around the bearing circumference in a total of five rows arranged across the bearing width. The oil passes through the ring channels and via the oil supply bores into the pockets of the bearing. Depending on the interconnection of the ring channels, the pads can be fed separately if required. The feeding pockets are placed directly at the pad leading edges to additionally reduce the friction power. The material parameters of the bearing are listed in Table 2. For emergency running properties, the bearing made of *C15* has a 6 mm thick babbitt layer made of *SnSb8Cu4*. While the coating is applied to both pads, it is missing in the deep groove areas.

Table 2. Material parameters of the bearing materials.

Parameter	Symbol	Material A *C15* Steel	Material B *SnSb8Cu4* Babbitt	Unit
Density	ρ	7870	7400	$kg \cdot m^{-3}$
Modulus of elasticity	E	205×10^9	56.5×10^9	$N \cdot m^{-2}$
Transverse contraction number	ν	0.28	0.33	1
Heat capacity	c_p	440	230	$J \cdot (kg \cdot K)^{-1}$
Thermal conductivity	λ	51.9	35	$W \cdot (m \cdot K)^{-1}$
Coefficient of thermal expansion	α	11×10^{-6}	23.4×10^{-6}	1

2.2. Test Rig for Large Hydrodynamic Journal Bearings

For the experimental investigation of the OHB test bearing, described in the previous Section 2.1, the large journal bearing test rig shown in Figure 2 is used. The test rig enables the experimental investigation of large journal bearings for turbine applications in original sizes [22]. The basic principle of the large journal bearing test rig is based on the so-called *floating bearing concept* in which the test bearing and shaft are displaced radially in relation to each other [38]. A summary of the most important test rig parameters is given in Table 3.

For measuring the maximum lubricant temperature T_{max} a total of 123 thermocouples is used, which are placed in the test bearing itself right under the running surface in the tangential and axial directions, as illustrated in Figure 2. Each of the total of 5 axial rows is 78 mm apart. The outermost rows start 20 mm from the bearing edge. Tangentially, there are 8 degrees between every two thermocouples, whereby the outer two rows only cover the lower pad. Unlike the temperature, the maximum lubricant film pressure p_{max} and the

minimum lubricant film thickness h_{min} are measured from the rotating and axially moving test shaft against the running surface of the test bearing. A total of four sensors is installed in the axial centre plane of the test shaft as seen in Figure 3.

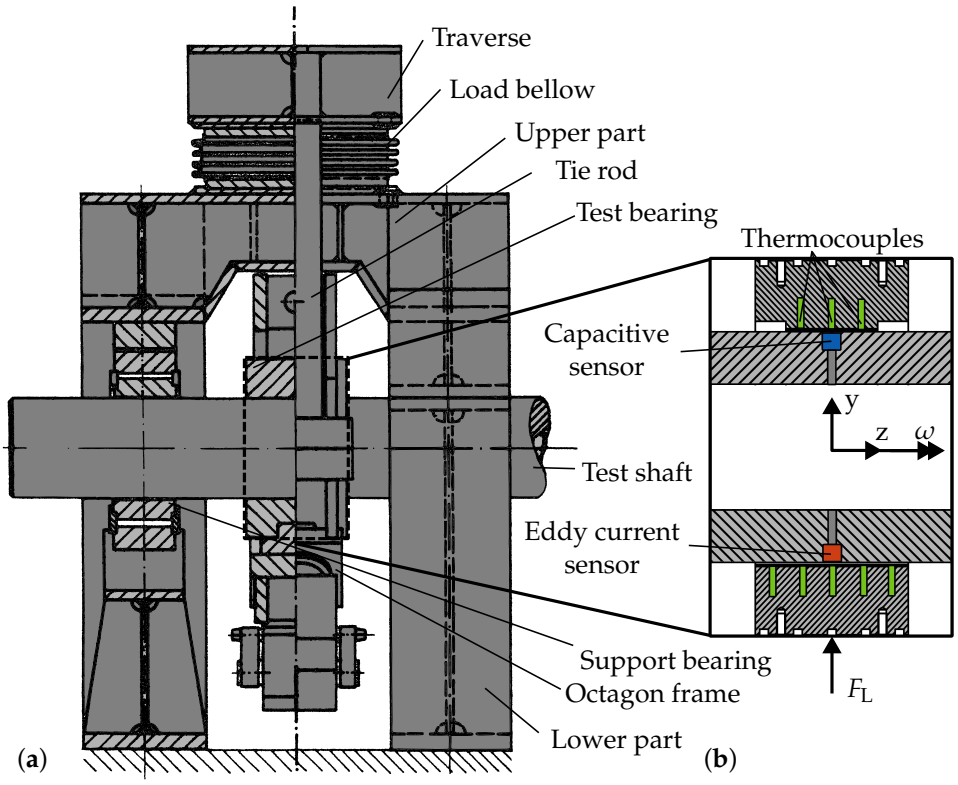


Figure 2. Test rig for large hydrodynamic journal bearings (side view); (**a**): test rig in radial half section; (**b**): enlarged view of the test bearing with measurement technology (radial section in the measuring plane of the distance sensors).

Table 3. Main parameters of the large journal bearing test rig.

Parameter	Sym.	Value	Unit
Test rig			
Shaft diameter	d	499.87	mm
Maximum test bearing width	b_{max}	500	mm
Stationary bearing load	F_L	0 to 1000	kN
Direct current motor			
Electrical power	P_{DC}	0 to 1200	kW
Speed range	n_{rng}	0 to 4000	min^{-1}
Minimum speed for hydrodynamic operation	n_{min}	200	min^{-1}
Axial shaft displacement	Δz_{MM}	0 to 550	mm
Oil supply system			
Tank volume	V_T	20,000	l
Low pressure volume (LP) flow rate	$\dot{V}_{ND}$	0 to 60	$l \cdot s^{-1}$
Volume flow high pressure (HP) supply test bearing	$\dot{V}_{NDpL}$	0 to 2	$l \cdot s^{-1}$

Two nominally redundant sensors are arranged 180° to each other. The measuring plane of the pressure sensors is offset from the measuring plane of the distance sensors by 90°. Both the redundant distance and pressure sensors record 240 measuring points per shaft revolution, triggered by an incremental encoder attached to the slip ring assembly. During the measurement, the shaft is axially moved through the bearing at a sufficiently slow speed rate so that the recorded measurement data can be viewed approximately as individual axial measurement planes from the actual spiral-shaped recording. A detailed

description of the test rig and a large part of the measurement technology installed to date can be found in [39].

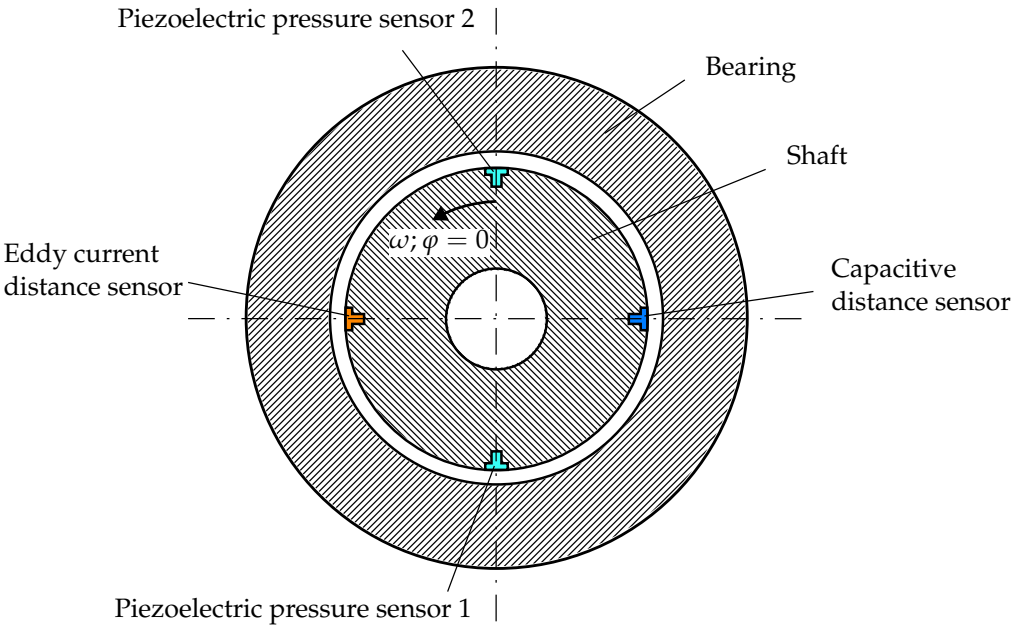


Figure 3. Schematic view: radial section of the shaft in the sensor plane.

2.3. Lubricant

The mineral oil *Esso Teresso 32* is used as lube oil for the tests in this investigation. Table 4 includes the most important thermohydrophysical parameters for various temperatures. The individual parameters were determined experimentally by the manufacturer.

Table 4. Material parameters *Esso Teresso 32*.

Symbol	**Value**							**Unit**
T	20	40	60	80	100	120	140	°C
ρ	856.1	843.5	830.8	818.0	805.1	792.1		$\mathrm{kg \cdot m^{-3}}$
η	89.14	35.15	17.52	10.19	6.62	4.65		mPa · s
ε		2.13	2.10	2.09				1
c	2032.7			2247.7	2319.3	2391.0	2462.7	$\mathrm{J \cdot (kg \cdot K)^{-1}}$
λ	0.134	0.134	0.134	0.134	0.134	0.134	0.134	$\mathrm{W \cdot (m \cdot K)^{-1}}$

Esso Teresso 32 has less than 5 vol.−% additives, which are mixed with the base mineral oil. Due to the low proportion of additives, the proportion of dissolved air V_g in the liquid phase of the lubricant V_l can be calculated via the *Bunsen coefficient* α_B using the *Henry–Dalton* law [40]:

$$V_\mathrm{g} = V_\mathrm{l} \frac{p_\mathrm{abs}}{p_\mathrm{atm}} \alpha_\mathrm{B} \tag{1}$$

The proportion of air already dissolved in the lubricant is therefore approximately 8% to 10%.

2.4. Deep Groove Void Fraction Variation and Identification

2.4.1. Deep Groove Void Fraction Variation

The variation of the deep groove void fraction is achieved by the design of a radially displaceable deep groove element that varies the groove depth as shown in Figure 4c.

Figure 4a shows the original design of the Offset Halves Bearing, described in Section 2.1. First, the deep groove is extended by the value Δw so that its total depth with the later inserted deep groove element corresponds to the initial depth, which can be seen in Figure 4b. Figure 4c the installed deep groove element is illustrated. Both guide rods with linear ball bearings are hollow and can be fed from the annular channel with the volume flow $\dot{V}_P$ independently of the volume flow $\dot{V}_L$. The adjustment mechanism will not be discussed further at this point. Therefore, the void fraction in the deep groove can either be varied by its depth h_P or the additional supply flow rate $\dot{V}_P$.

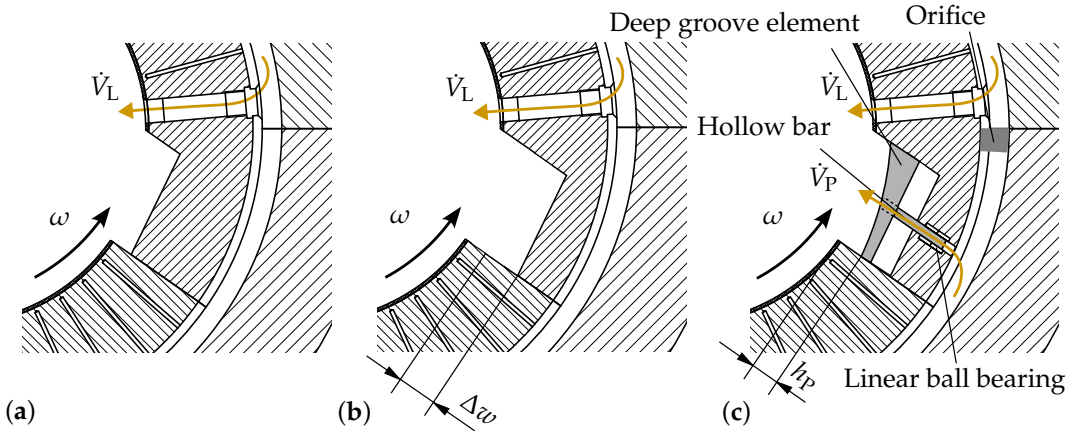


Figure 4. Radially adjustable deep groove elements, which can be fed with lubricant; (**a**): initial design; (**b**): recessed deep groove; (**c**): recessed deep groove with deep groove element.

The deep groove element, which can be adjusted by h_P during operation, can be moved radially in the range

$$h_P \in [0, 45] \ \text{, mm} \tag{2}$$

where the deep groove element at $h_P = 0$ is flush with the pad radius R_S of the upstream pad. The volume flow $\dot{V}_P$ can be varied in the range of

$$\dot{V}_P \in [0, 5] \ \text{, L} \cdot \text{s}^{-1} \tag{3}$$

A low void fraction can be achieved by reducing h_P and increasing $\dot{V}_P$, as this decreases the area between the deep groove elements and the shaft and floods it at the same time. To increase the void fraction, the opposite applies.

2.4.2. Deep Groove Void Fraction Identification

The camera system *Arducam 16MP IMX519 Synchronised Quad-Camera Kit*, exemplarily shown in Figure 5 for the lower deep groove and the ring groove of the upper pad, is used to qualitatively identify the void fraction of the areas outside the lubrication gap.

A total of 8 cameras with 16 megapixels each and manually adjustable focus are used and operated with 2 *Raspberry Pi 4B*. While the radial filming cameras are placed in the deep groove elements behind plexiglass and move with the radial adjustment of h_P, the cameras for the ring groove remain fixed in place.

2.5. Lubrication Gap Void Fraction Variation and Identification

2.5.1. Lubrication Gap Void Fraction Variation

The variation of the lubrication gap void fraction is achieved by varying the amount of oil at the leading edges of the pads. Figures 1 and 4 show an example of how $\dot{V}_L$ is fed to the pad via a wide pocket at the pad's leading edges.

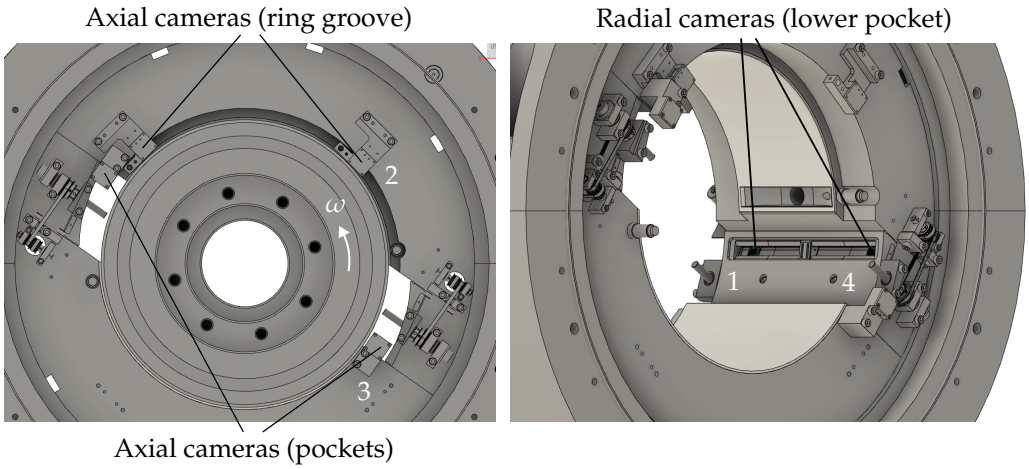


Figure 5. Camera system for identifying the lower deep groove and ring groove void fraction; *1,4*: radial cameras in deep groove element; *2,3*: axial cameras for the ring groove void fraction.

2.5.2. Lubrication Gap Void Fraction Identification

In comparison to the qualitative recording of the deep groove void fraction the gap void fraction is determined quantitatively. The mathematical model presented here is based on the idea of a two-phase material between the two plates of an ideal plate capacitor. In reality, this model assumption corresponds to the area between the capacitive distance sensor and the bearing shell. Assuming that only oil with the relative permittivity ε_l and air with the relative permittivity ε_g can be present in the lubrication gap, various assumptions can be made regarding the distribution and characteristics of the air content in the oil. Figure 6 shows the three discussed approaches to determine the fractional film content via the effective relative permittivity $\bar{\varepsilon}$ in this investigation:

- Parallel distribution of oil and air:

$$\theta_{pd} = (\bar{\varepsilon} - 1)(\varepsilon_l - 1)^{-1} \tag{4}$$

- Serial distribution of oil and air:

$$\theta_{sd} = (\bar{\varepsilon} - \varepsilon_g)(\varepsilon_l - \varepsilon_g)^{-1} \tag{5}$$

- Disperse distribution of oil and air according to *Bruggeman* [41]:

$$\theta_{ddBM} = 1 - ((-\varepsilon_l + \bar{\varepsilon})(\varepsilon_l + 2\bar{\varepsilon})^{-1}) \cdot ((\varepsilon_g - \bar{\varepsilon})(\varepsilon_g + 2\bar{\varepsilon})^{-1} - (\varepsilon_l - \bar{\varepsilon})(\varepsilon_l + 2\bar{\varepsilon})^{-1})^{-1} \tag{6}$$

Since partially filled or empty bearing areas are usually associated with the phenomenon of cavitation, a largely dispersed distribution of air in the oil is assumed. According to Figure 6, the effective medium approach according to Bruggeman represents a good balance between the parallel circuit approach and the series circuit approach.

To determine the void fraction θ_{ddBM}, it is necessary to know the partial dielectricities ε_l and ε_g as well as the effective relative permittivity $\bar{\varepsilon}$ composed of the liquid and gaseous phases. For this purpose, two redundant distance sensors with different measuring principles, which can be seen in Figure 7, are used.

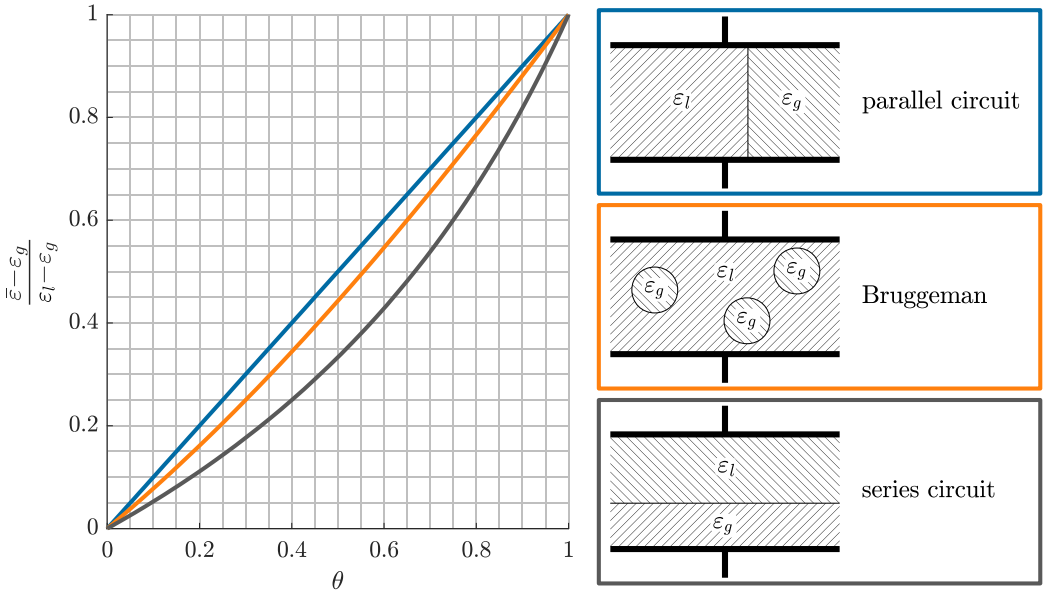


Figure 6. Comparison of the models for determining the void fraction.

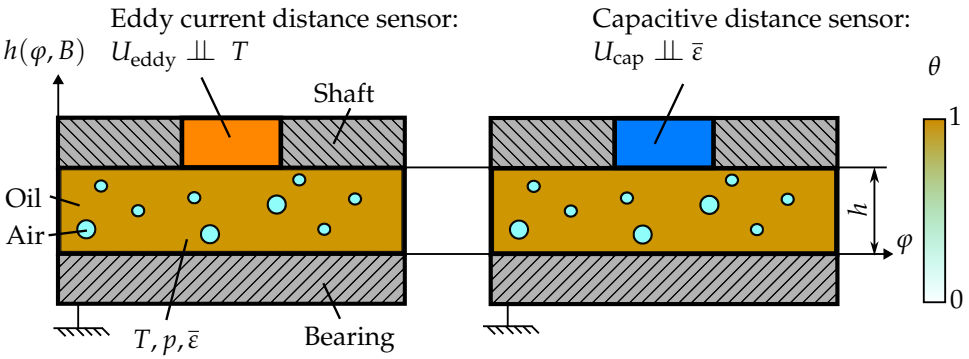


Figure 7. Comparison and dependencies of the distance sensors.

In the example shown, both sensors measure the distance at the same time and at the same circumferential and axial position in the lubrication gap. The medium between the sensor surface and the bearing surface is a mixture of the lubricant described in Section 2.3 with dispersed air inclusions. While the eddy current sensor measures the distance as a function of the temperature but independently of the relative permittivity, the capacitive sensor signal is affected by the change in dispersed air. First, the capacitive distance sensor is calibrated in air so that a relationship is established between the distance and the voltage. During operation, the capacitive distance sensor then measures the distance as a function of the oil–air mixture, which changes the output voltage value but not the approximate linear behavior. From these considerations, a model for determining the overall relative permittivity can be established:

For the capacitive distance measurement in air and in the mixture of oil and air, the charge remains the same:

$$C_g \cdot U_g = \overline{C} \cdot \overline{U}. \tag{7}$$

The relationship between capacitance and the relative permittivity is given by

$$C = \varepsilon_0 \cdot \varepsilon \cdot \frac{A}{h}. \tag{8}$$

Substituting Equation (7) into Equation (8) leads to the expression

$$\bar{\varepsilon} = \frac{\varepsilon_g U_g}{\overline{U}}. \tag{9}$$

If the assumption is made that $\varepsilon_g \neq f(T, \mu_{dipole})$ it can be assumed that $\varepsilon_g \cdot \varepsilon_0^{-1} \approx 1$ so that

$$\bar{\varepsilon} = \frac{U_g}{\overline{U}}. \tag{10}$$

The capacitive distance sensor, which was previously calibrated in air, has the characteristic curve shown in Figure 8. If the sensor calibrated in air measures the distance in the oil–air mixture, the voltage $\overline{U}$ is output, which no longer describes the true distance due to the change in relative permittivity. Using the relationship described in Equation (10), the eddy current sensor, which describes the distance independently of the relative permittivity, can be used to determine the voltage U_g that the capacitive distance sensor would display at the same distance in air.

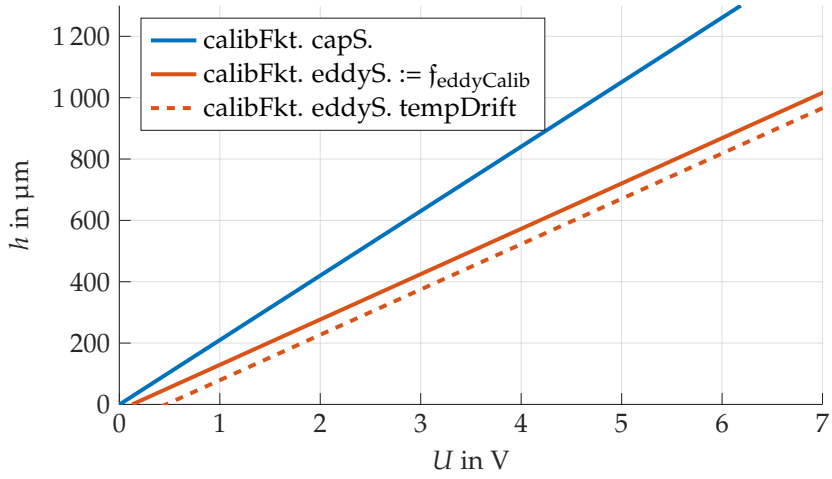
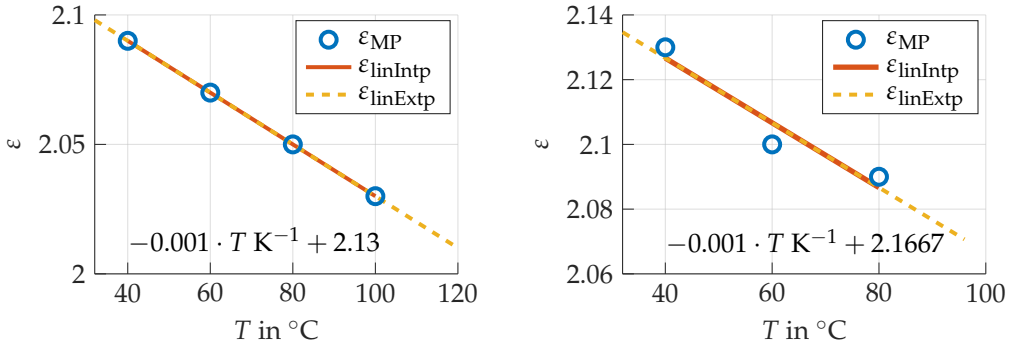


Figure 8. Calibration functions of the capacitive distance sensor and the eddy current distance sensor.

The temperature drift of the eddy current sensor corresponds to a shift of the y-axis section in the negative ordinate direction of the calibration function, so it can be assumed that

$$U_{eddy}(h) = f_{eddyCalib} + \left(U_{cap}(h_{min}) - U_{eddy}(h_{min})\right). \tag{11}$$

Finally, the last missing variable to derive θ_{ddBM} from the experimental data is the dielectric constant of oil ε_{VG32} as a function of temperature. For this purpose, the measured temperature-dependent dielectricities of two VG32 lubricants from different manufacturers are compared in Figure 9. Despite the small number of measuring points of *Esso Teresso 32* in Figure 9b, the linear character of the relative permittivity can be determined when comparing it with the similar *Shell Turbo GT 32* lubricant in Figure 9a.



(**a**) Relative permittivity as a function of the temperature of *Shell Turbo GT 32*

(**b**) Relative permittivity constant as a function of the temperature of *Esso Teresso 32*

Figure 9. Relative permittivity as a function of temperature of different VG 32 lubricants.

3. Results

The stationary tests are carried out at various operating points, which are summarised in Table 5. The selected rotational speeds and specific bearing loads represent typical operating points for large hydrodynamic journal bearings used in steam and gas turbines in terms of line frequency and rotor weight.

Table 5. Experimental plan with operating points.

n in min^{-1}	$\overline{p}$ in MPa	$\dot{V}_\mathrm{L}$ in $\mathrm{L \cdot s^{-1}}$	$\dot{V}_\mathrm{P}$ in $\mathrm{L \cdot s^{-1}}$	T_sup in °C	h_P in mm
1500	0.5, 1.0...4.0	7.5	0.0, 0.5...2.5	50	45, 10, 8, 6...0
3000	1.0, 1.5...5.0	7.5	0.0, 0.5...4	50	45, 10, 8, 6...0
3600	1.0, 1.5...4.5	7.5	0.0	50	45

$h_\mathrm{P} = 45$ mm =: Deep grooves are fully opened
$h_\mathrm{P} = 0$ mm =: Deep grooves are fully closed
$\dot{V}_\mathrm{L} = 7.5\ \mathrm{L \cdot s^{-1}}$ =: Nominal oil volume flow rate

3.1. Deep Groove Void Fraction

Initially, the deep groove elements are moved radially towards the shaft during the tests to investigate the influence of the deep groove void fraction on operational safety and power loss. In addition, an attempt is made to flood the deep grooves with lubricant. Images of the lower groove camera system are shown as an example in Figure 10. The numbers in the headings of the subfigures correspond to the denomination for the location of each camera in Figure 5. Cameras (**1**) and (**4**) film directly onto the rotating shaft through the plexiglass screen of the deep groove element. Despite the lighting, only different shades of yellow of the oil are visible. The same applies to camera (**2**), which films axially into the ring groove. The images from camera (**3**) are the only representative images. On the one hand, the lubricant adhering to the shaft can be seen, which is transported in strands from the lower to the upper pad. An oil plateau in the bottom right-hand edge of the deep groove can be identified. In principle, it can be observed that the deep grooves are not filled under any conditions, regardless of speed, load, and amount of lubricant supplied to the leading edges of the pads. Even moving the deep groove elements right to the edge of the adjoining pad does not lead to a reduction in operational reliability, shown in Figures 11a and 12a,b, or an increase in power loss, which is shown in Figure 11b. Fluctuations are within the range of measurement accuracy. With regard to operational safety, a slight decrease of the maximum temperature is the only recognisable trend. Given the comparably low impact of the deep groove depth on steady-state operational reliability and power loss, the lubrication gap void fraction is the sole parameter subjected to further analysis in Section 3.2. However,

the impact of the void fraction in the deep groove on dynamic operating conditions might be different and needs to be investigated separately.

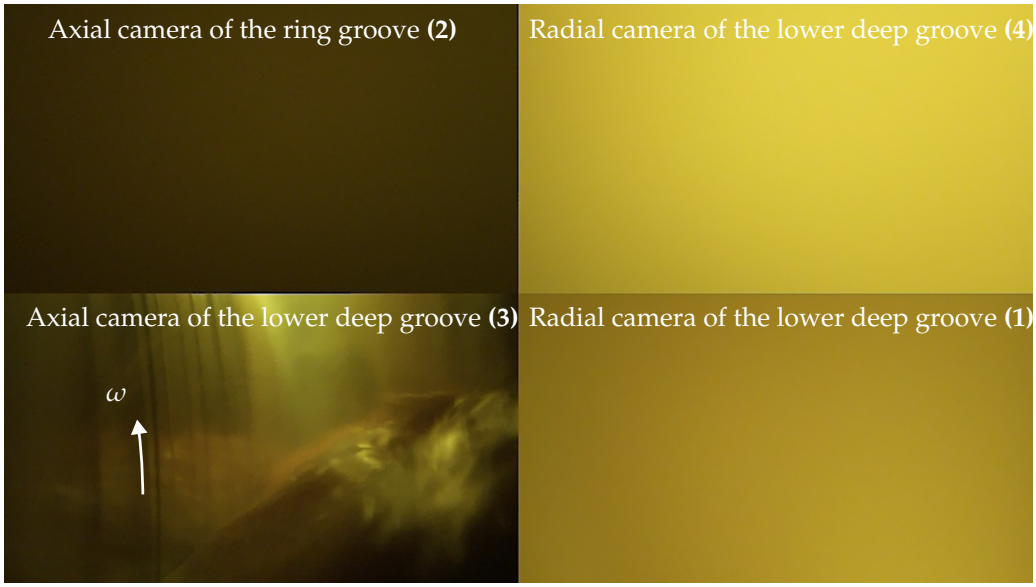
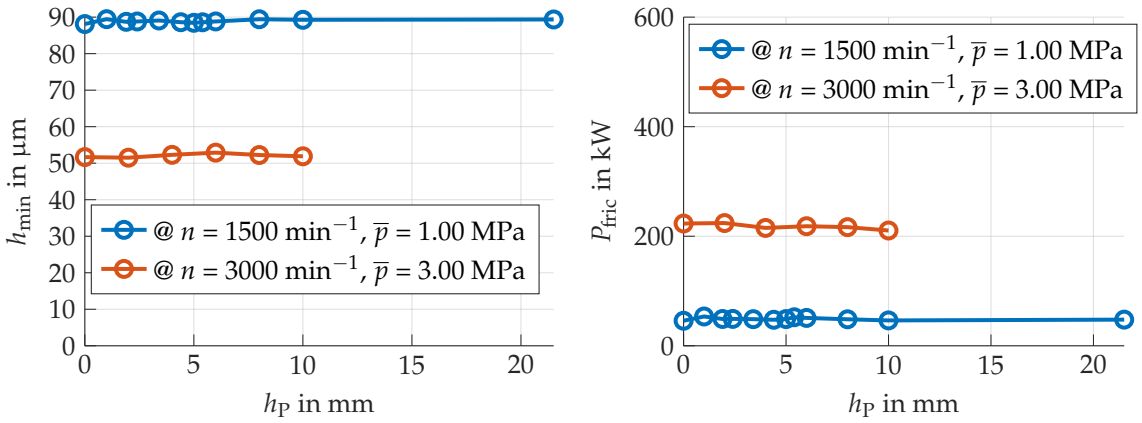


Figure 10. Deep groove void fraction @ $n = 1500\ \mathrm{min}^{-1}$, $\overline{p} = 1.00$ MPa, $h_\mathrm{P} = 45$ mm, $\dot{V}_\mathrm{L} = 7.5\ \mathrm{L} \cdot \mathrm{s}^{-1}$.



(**a**) Minimum lubricant film thickness as a function of deep groove depth

(**b**) Frictional power loss as a function of deep groove depth

Figure 11. Deep groove depth influence on h_min and P_fric at different operating points.

3.2. Lubrication Gap Void Fraction

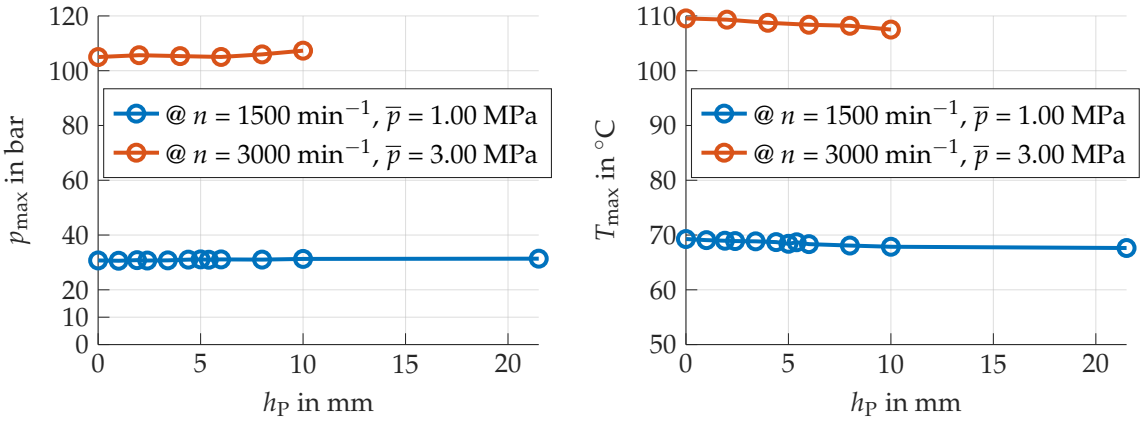
The results of the quantitative measurement of the void fraction at two extreme operating points are presented in Figure 13. They show the distribution of oil and air at low rotational speed and load in Figure 13a and high rotational speed and load in Figure 13a. The two cases differ by an approximate fully filled lubrication gap in (**a**) and a very high air content in (**b**). In the following, the abbreviation lgvf is used for "lubrication gap void fraction" and lgpd for "lubrication gap pressure distribution". The area cut out in the centre is the hydrostatic lifting pocket, which is described in more detail below. As can be seen from the colour scale in the figures on the right, the lubrication gap *fractional film content* is defined by

$$\theta \in [0, 1], \tag{12}$$

Thus, the *void fraction* is defined by

$$(1-\theta) \in [0,1], \tag{13}$$

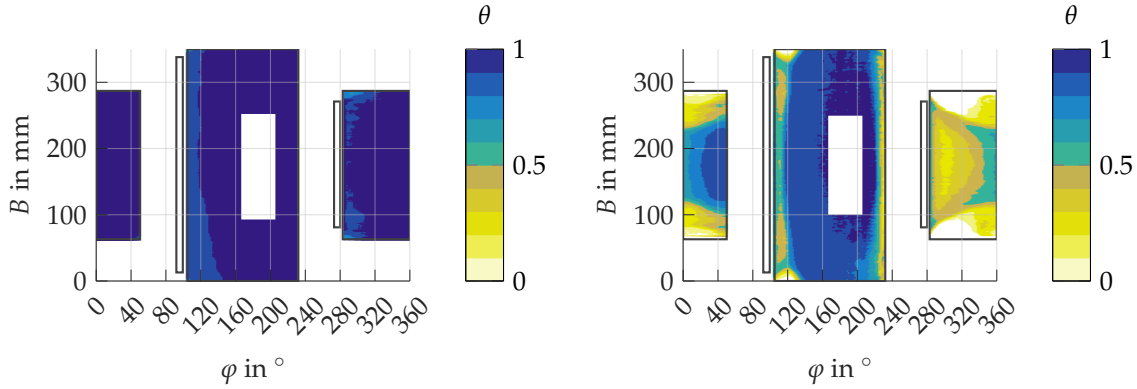
where $\theta = 0$ is a complete absence of oil and $\theta = 1$ is a complete absence of gas or vapour.



(**a**) Maximum lubricant film pressure as a function of deep groove depth

(**b**) Maximum lubricant film temperature as a function of deep groove depth

Figure 12. Deep groove depth influence on operational safety and power loss at different operating points.



(**a**) lgvf @ $n = 1500$ min^{-1}, $\overline{p} = 0.50$ MPa

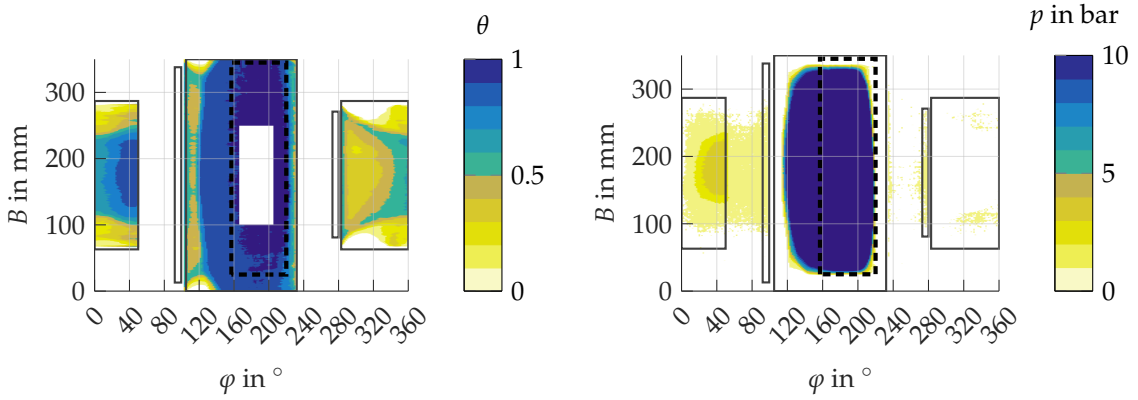
(**b**) lgvf @ $n = 3600$ min^{-1}, $\overline{p} = 4.50$ MPa

Figure 13. Lubrication gap void fraction at low rotational speed and load (**a**) and high rotational speed and load (**b**) under standard oil supply and fully opened deep grooves.

The direction of rotation is in the positive φ-direction. In the centre, from $\varphi = 104°$ to $\varphi = 231°$, the lower loaded pad can be seen, which has been slightly shortened tangentially because the distance sensor signals at the leading and trailing edge of the pad exceed the maximum measuring range. This principle encompasses the upper, unloaded pad, which is shown as a section from $\varphi = 284°$ to $\varphi = 52°$. The deep groove areas in the spaces between the pads and the hydrostatic lift pocket in the middle of the loaded pad are cut out as well because of their depth. It is noticeable that the void fraction is growing significantly with increasing speed and load. In particular, the air fraction rises at the leading and trailing edges of the loaded pad and at the leading edge of the unloaded pad. In both pads, particularly at the beginning of the pad, there are high *air entrainment* areas at the axial edges, which decrease towards the trailing edge. Whereas in Figure 13a almost the entire running surface of both pads is completely filled with oil, the area without air content in Figure 13b is limited to a range of $\varphi = 160°$ to 220°. This area is located directly behind the

location of the minimum lubricant film thickness, in the area of the maximum lubricating film pressure.

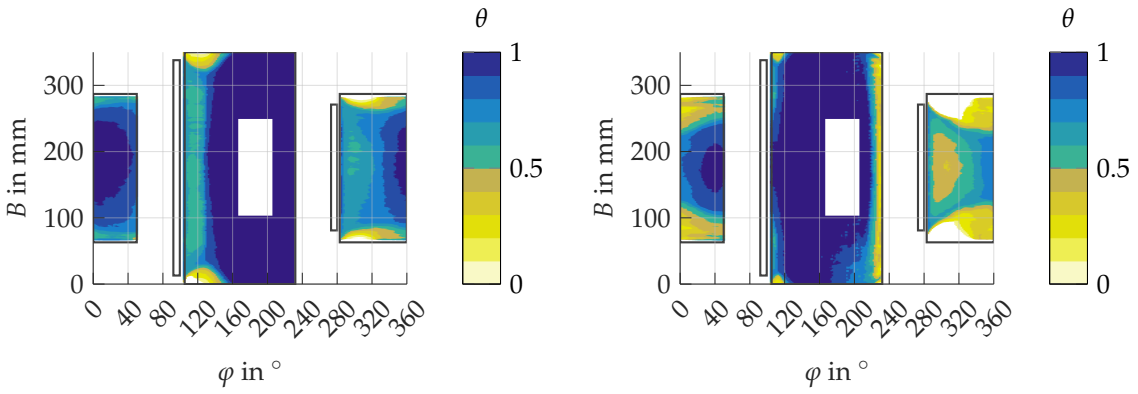
A comparison of the void fraction distribution depicted in Figure 14a with the lubricant pressure distribution illustrated in Figure 14b reveals that there is also a void fraction of $\theta > 0$ in regions exhibiting pressures that are significantly above atmospheric pressure. The area enclosed by the dashed line represents the region of absolute void filling of $\theta = 1$. It is notable that there are areas surrounding this region with pressures exceeding 10 bar, where the fractional film content of θ is observed to be between 80% and 90%.



(**a**) lgvf @ $n = 3600\ \text{min}^{-1}, \overline{p} = 3.50$ MPa (**b**) lgpd @ $n = 3600\ \text{min}^{-1}, \overline{p} = 3.50$ MPa

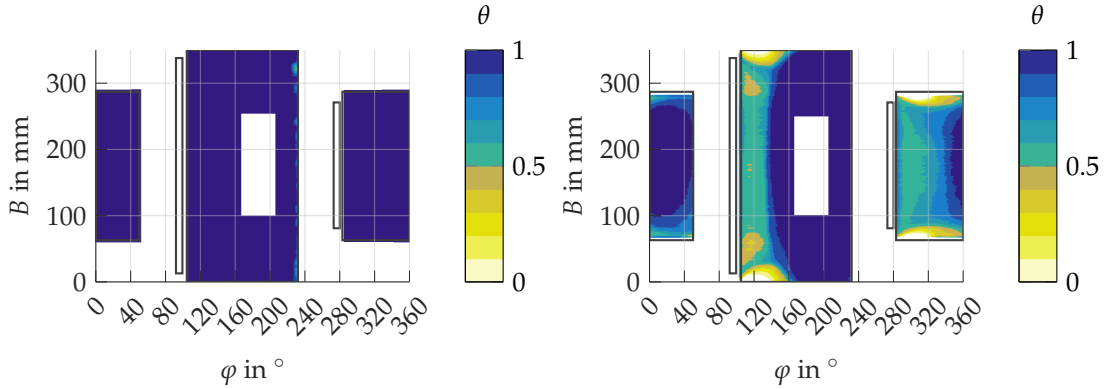
Figure 14. Lubrication gap pressure distribution (**a**) and void fraction (**b**) under standard oil supply and fully opened deep grooves.

Figure 15 shows the impact of increasing load on the fractional film content at a rotor speed of 3000 min^{-1}. From (**a**) to (**b**) the proportion of air increases, and the highest air content shifts from the leading to the trailing edge of the loaded pad. The upper, unloaded pad is even less filled with oil at high loads. According to Figure 15b, an overall larger area of the loaded pad is filled with pure oil, while at the trailing edge of the pad a high void fraction is present. In Figure 16 an increase of the void fraction is observable, due to an increase in rotational speed at a constant load of $\overline{p} = 1.00$ MPa. While the lubrication gaps of both pads are almost completely filled with oil at $n = 1000\ \text{min}^{-1}$, the void fraction is high at $n = 3600\ \text{min}^{-1}$. In contrast to the load increase from Figure 15, this clearly shows that the void fraction increases particularly at the beginning of the loaded pad and at the end of the unloaded pad. Around two-thirds of the loaded pad, behind the partially filled area at the leading edge, are completely filled with oil.



(**a**) lgvf @ $n = 3000\ \text{min}^{-1}, \overline{p} = 1.00$ MPa (**b**) lgvf @ $n = 3000\ \text{min}^{-1}, \overline{p} = 4.50$ MPa

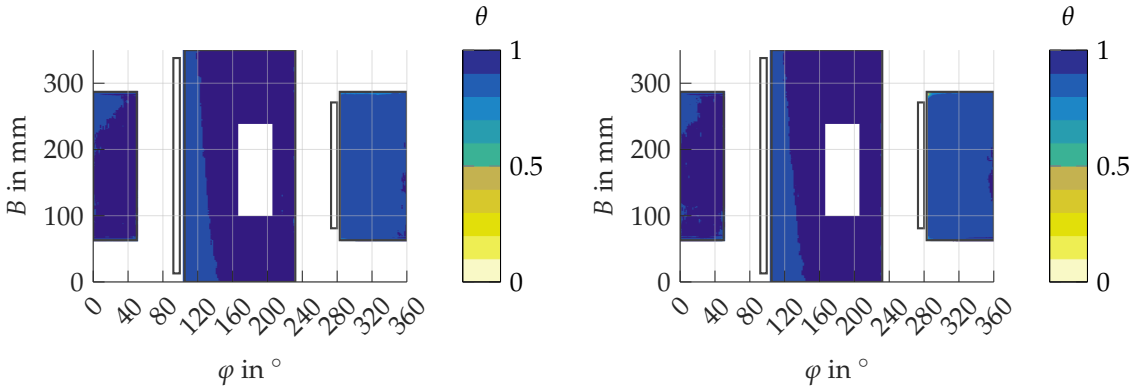
Figure 15. Lubrication gap void fraction @ $n = 3000\ \text{min}^{-1}$, $\overline{p} = 1.00...4.50$ MPa with standard oil supply and fully opened deep grooves.



(**a**) lgvf @ $n = 1000\ \mathrm{min}^{-1}, \overline{p} = 1.00$ MPa (**b**) lgvf @ $n = 3600\ \mathrm{min}^{-1}, \overline{p} = 1.00$ MPa

Figure 16. Lubrication gap void fraction @ $n = 1000..3600\ \mathrm{min}^{-1}$, $\overline{p} = 1.00$ MPa with standard oil supply at maximum deep groove depth.

Figure 17 depicts the influence of additional lubrication by means of the oil supply through the deep groove element in the space between the pads region. In Figure 17a the operating point can be seen with fresh oil flow rate increased by $2.0\ \mathrm{L \cdot s^{-1}}$ to $\dot{V}_\mathrm{L} = 9.5\ \mathrm{L \cdot s^{-1}}$. The gap, which is approximately fully filled at $\dot{V}_\mathrm{L} = 7.5\ \mathrm{L \cdot s^{-1}}$, does not have a visibly reduced void fraction. In (**b**), the deep groove feed rate of $\dot{V}_\mathrm{P} = 3.0\ \mathrm{L \cdot s^{-1}}$ is used in addition to $\dot{V}_\mathrm{L}$. The already filled gap also shows no noticeable change in the void fraction.

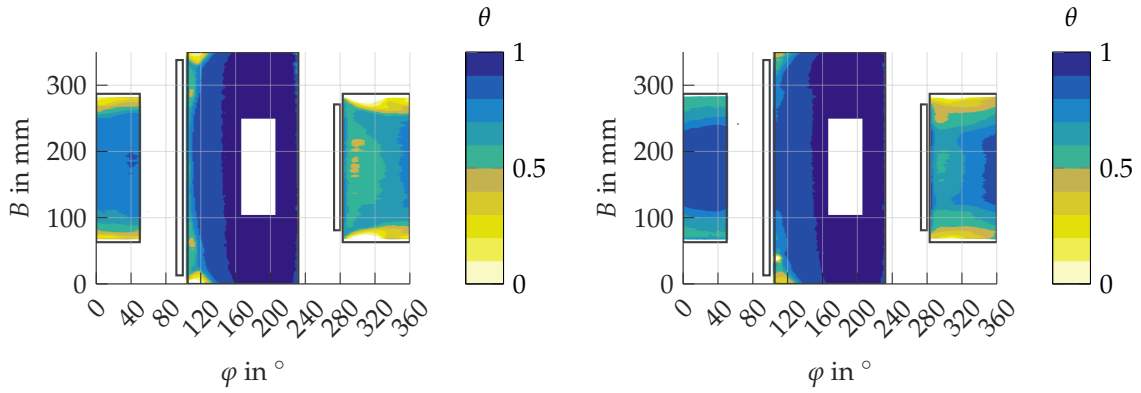


(**a**) lgvf @ $n = 1500\ \mathrm{min}^{-1}, \overline{p} = 1.00$ MPa, $\dot{V}_\mathrm{L} = 9.5\ \mathrm{L \cdot s^{-1}}, \dot{V}_\mathrm{P} = 0.0\ \mathrm{L \cdot s^{-1}}$

(**b**) lgvf @ $n = 1500\ \mathrm{min}^{-1}, \overline{p} = 1.00$ MPa, $\dot{V}_\mathrm{L} = 9.5\ \mathrm{L \cdot s^{-1}}, \dot{V}_\mathrm{P} = 3.0\ \mathrm{L \cdot s^{-1}}$

Figure 17. Lubrication gap void fraction @ $n = 1500\ \mathrm{min}^{-1}$, $\overline{p} = 1.00$ MPa with varying $\dot{V}_\mathrm{P}$.

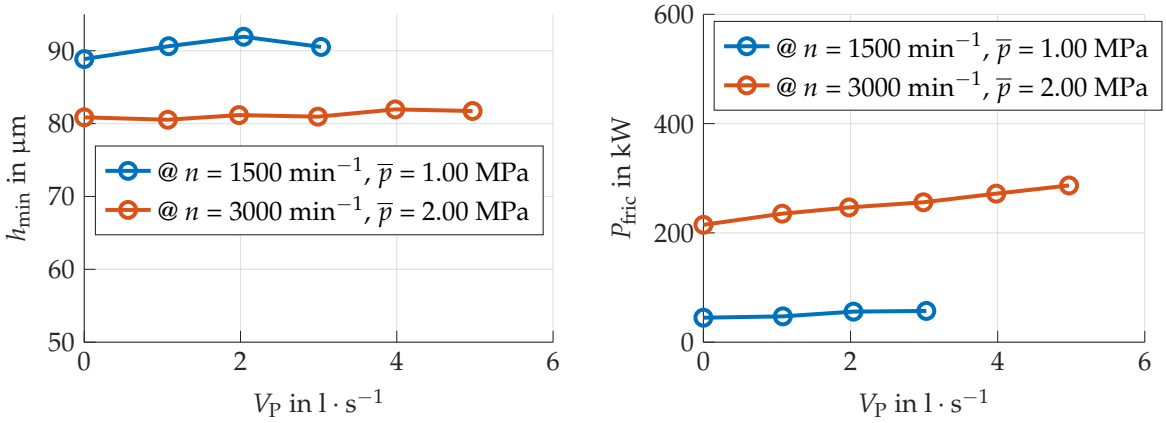
For the operating points shown in Figure 18, a similar procedure was followed as previously in Figure 17. Here, the standard oil flow rate of $\dot{V}_\mathrm{L} = 7.5\ \mathrm{L \cdot s^{-1}}$ at the pockets of the pads leading edges and the oil flow rate of the deep grooves were increased from $\dot{V}_\mathrm{P} = 0.0\ \mathrm{L \cdot s^{-1}}$ in Figure 18a to $\dot{V}_\mathrm{P} = 5.0\ \mathrm{L \cdot s^{-1}}$ in (**b**). A slight reduction in the void fraction can be seen, both in the loaded and in the unloaded pad. Figures 19 and 20 include characteristic parameters for the operational reliability and power loss as a function of the oil supply volume flow rate of the pockets. While no noticeable influence of $\dot{V}_\mathrm{P}$ can be recognised with $n = 1500\ \mathrm{min}^{-1}$ and $\overline{p} = 1.00$ MPa, at $n = 3000\ \mathrm{min}^{-1}$ and $\overline{p} = 2.00$ MPa, there is a trend towards an increase in power loss with a simultaneous slight reduction in maximum temperature as the oil flow rate increases.



(**a**) lgvf @ $n = 3000\ \mathrm{min}^{-1}, \overline{p} = 1.00$ MPa, $\dot{V}_\mathrm{L} = 7.5\ \mathrm{L \cdot s}^{-1}, \dot{V}_\mathrm{P} = 0.0\ \mathrm{L \cdot s}^{-1}$

(**b**) lgvf @ $n = 3000\ \mathrm{min}^{-1}, \overline{p} = 2.00$ MPa, $\dot{V}_\mathrm{L} = 7.5\ \mathrm{L \cdot s}^{-1}, \dot{V}_\mathrm{P} = 5.0\ \mathrm{L \cdot s}^{-1}$

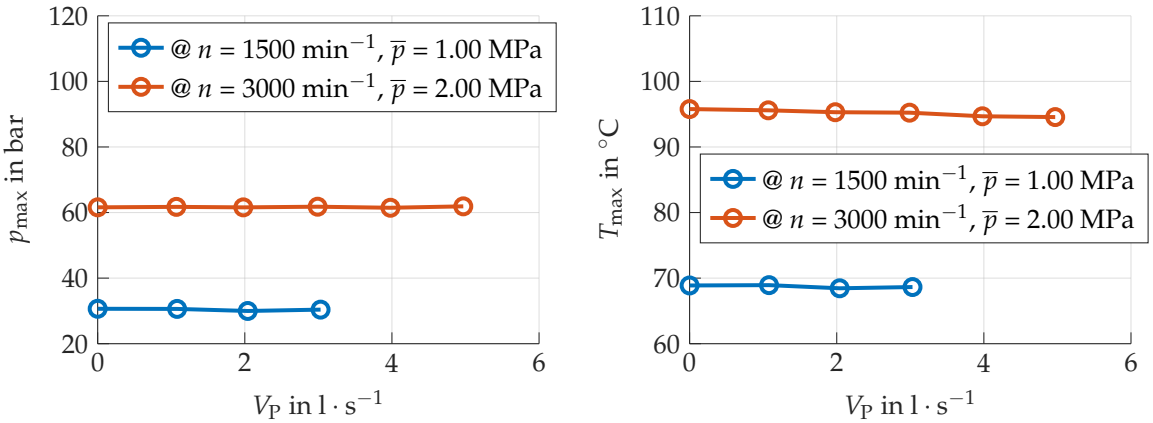
Figure 18. Lubrication gap void fraction @ $n = 3000\ \mathrm{min}^{-1}, \overline{p} = 2.0$ MPa with varying $\dot{V}_\mathrm{P}$.



(**a**) Minimum lubricant film thickness as a function of deep groove flow rate

(**b**) Frictional power loss as a function of deep groove flow rate

Figure 19. Deep groove volume flow influence on h_min and P_fric at different operating points.



(**a**) Maximum lubricant film pressure as a function of deep groove flow rate

(**b**) Maximum lubricant film temperature as a function of deep groove flow rate

Figure 20. Deep groove flow rate influence on maximum film pressure and temperature at different operating points.

4. Conclusions

This paper presents a novel approach to identify the *void fraction* in a hydrodynamic journal bearing. The investigations can be divided into two parts:

- Qualitative identification of the void fraction in the deep grooves via a camera system.
- Quantitative identification of the void fraction in the lubrication gap via a novel approach based on a combination of eddy-current and capacitive sensors.

The void fraction in the deep grooves, which can be adjusted in depth by a specially designed mechanism, demonstrates that there is no impact on the overall operational behaviour, irrespective of the depth set. This is due to the fact that a near-total transfer of oil from the trailing edge of the preceding pad to the trailing edge of the subsequent pad occurs, resulting in the deep grooves being almost entirely unfilled at any given operating point. Consequently, no pressure build-up occurs between the shaft and the deep grooves, and thus no shear stress is generated. Furthermore, the measured operational safety indicates no notable alterations. Additional flooding of the deep grooves will only add lubricant to the subsequent lubrication gap unless it is already completely filled. It can therefore be concluded that the deep groove areas have no significant impact on the static operating behaviour of the bearing.

The second part of the void fraction investigation concentrates on the lubrication gap, which dominates the bearing operating behaviour due to the negligible influence of the deep groove void fraction determined above. The following key points can be made from the results of the investigations:

- It has been demonstrated that cavitation phenomena can also occur in the lubricating film at pressures above atmospheric pressure. Furthermore, all stationary tests have shown that *stable cavitation conditions* can be achieved, which means that the void fraction does not change at the respective operating point, even after minutes of measurements at several thousand revolutions. In addition, no damage to the bearing could be detected. Thus, the main mechanism, therefore, appears to be *gaseous* or *pseudo cavitation*, although further investigations are required.
- The void fraction is characterised by different levels of air in the lubrication gap, originating partly from circumferential and axial *air entrainment* and partly from air dissolved in the lubricant.
- As the specific bearing load increases, the void fraction shifts from the leading edge to the trailing edge of the pad, particularly at higher speeds, as the distance between the shaft and bearing decreases and the eccentricity of the shaft increases. This leads to divergent gap areas at the pad, where the void fraction elevates.
- With increasing rotational speed, the void fraction of the loaded pad increases considerably for the same load. This is due, on the one hand, to the greater distance between the shaft and the pad surface as a result of the decreased eccentricity and, on the other hand, to the circumferential shaft speed, which favours cavitation.
- The void fraction is significantly related to the friction power converted in the bearing. In the case of lubrication gaps that are already fully filled, it can be seen that no more noticeable shear stress is converted when more oil is added.

Further research is required to gain a deeper understanding of the cavitation phenomena in the lubrication gap. Firstly, the void fraction in different bearing designs should be investigated in order to compare them with the results of the Offset Halves Bearing study. In addition, the general influence of the void fraction on operational safety and power loss, which are particularly relevant to practical operation, was to be investigated. The method of *starved lubrication*, which can be applied in this context, leads to high void fractions in the lubrication gap areas, which significantly reduce power loss. However, the processes that take place in the lubrication gap under greatly reduced oil volumes have not yet been visualised or sufficiently understood. Finally, the methods developed in this publication have only been used to examine journal bearings in a stationary operating state, so the void fraction should also be investigated under *dynamic operating conditions*.

Author Contributions: Conceptualization and methodology, A.E., M.S., S.W. and T.H.; software, A.E. and M.S.; validation, A.E. and M.S.; formal analysis, A.E. and S.W.; investigation, A.E., M.S., S.W. and T.H.; resources and data curation, A.E. and M.S.; writing original draft preparation, A.E., S.W. and T.H.; writing review and editing, M.S., C.W., B.B. and H.S.; visualization, A.E.; supervision and funding acquisition, C.W., B.B. and H.S. All authors have read and agreed to the published version of the manuscript.

Funding: This research was funded by the German Federal Ministry of Economic Affairs and Climate Action. The financial support was assigned by the Industrial Research Association (AiF e.V.) in project number IGF 21389 N.

Data Availability Statement: Data is contained within the article.

Conflicts of Interest: Author Christoph Weißbacher was employed by the company Gleitlagertechnik Weißbacher GmbH. The remaining authors declare that the research was conducted in the absence of any commercial or financial relationships that could be construed as a potential conflict of interest.

Nomenclature

Symbols

A	surface area
α	coefficient of thermal expansion
α_{B}	Bunsen coefficient
b_{b}	width of the loaded pad
b_{max}	maximum test bearing width
b_{ub}	width of the unloaded pad
C	capacitance of an ideal plate capacitor
C_{g}	capacitance of an ideal plate capacitor in air
C_{l}	capacitance of an ideal plate capacitor in oil
$\overline{C}$	capacitance of an ideal plate capacitor in two-phase mixture
c_p	specific heat capacity
d	shaft diameter
$\Delta\, z_{\mathrm{MM}}$	displacement
Δw	deep groove depth extension
E	Young's modulus
ε	relative permittivity
ε_{g}	relative permittivity of the gaseous phase
ε_{l}	relative permittivity of the liquid phase
$\overline{\varepsilon}$	effective relative permittivity
η	dynamic viscosity
F_{L}	stationary bearing load
$\mathrm{f}_{\mathrm{eddyCalib}}$	calibration function of the eddy current distance sensor
h	film thickness
h_{min}	minimum lubricant film thickness
h_{P}	deep groove depth
λ	thermal conductivity
n	rotational speed
n_{min}	minimum speed
n_{rng}	speed range
ν	lateral contraction number (Poisson's Ratio)
ω	angular velocity
P_{DC}	electrical power
p	pressure
p_{abs}	absolute pressure
p_{atm}	atmospheric pressure

p_{max}	maximum lubricant film pressure
$\overline{p}$	specific bearing load
Ψ_i	relative bearing clearance
Ψ_v	preload factor
P_{fric}	power loss
R_a	outer bearing radius
R	inner bearing radius
R_S	pad radius
ρ	density
T	temperature
θ	fractional film content
θ_{ddBM}	calculated fractional film content for disperse distribution of oil and air (Bruggeman)
θ_{ddMG}	calculated fractional film content for disperse distribution of oil and air (Maxwell-Garnett)
θ_{LG}	fractional film content of the lubrication gap
θ_{pd}	calculated fractional film content for parallel distribution of oil and air
θ_{sd}	calculated fractional film content for serial distribution of oil and air
T_{max}	maximum lubricant film temperature
T_{sup}	supply temperature of the lubricant
U	voltage of an ideal plate capacitor
U_g	voltage of an ideal plate capacitor in air
U_{cap}	voltage of capacitive distance sensor
U_{eddy}	voltage of eddy current distance sensor
U_l	voltage of an ideal plate capacitor in oil
$\overline{U}$	voltage of an ideal plate capacitor in two-phase mixture
φ_{inst}	installation angle
φ	circumferential angle
V_g	volume fraction of gas phase
V_l	volume fraction of liquid phase
$\dot{V}_L$	volume flow rate of the leading edges (in total)
$\dot{V}_{ND}$	low pressure volume flow rate
$\dot{V}_{NDpL}$	volume flow high pressure supply test bearing
$\dot{V}_P$	volume flow rate of the deep grooves (in total)
V_T	tank volume

Abbreviations

OHB	Offset Halves Bearing
calibFkt.	calibration function
capS.	capacitive distance sensor
eddyS.	eddy current distance sensor
tempDrift	temperature drift
MP	measurement point
linIntp	linear interpolation
linExtrp	linear extrapolation
lgvf	lubrication gap void fraction
lgpd	lubrication gap pressure distribution

References

1. IPCC (Intergovernmental Panel on Climate Change). *Global Warming of 1.5° C. An IPCC Special Report on the Impacts of Global Warming of 1.5° C above Pre-Industrial Levels and Related Global Greenhouse Gas Emission Pathways, in the Context of Strengthening the Global Response to the Threat of Climate Change, Sustainable Development, and Efforts to Eradicate Poverty*; Ipcc: Geneva, Switzerland, 2018.
2. Vine, D.; Henderson, C. Clean Heat Pathways for Industrial Decarbonization. In *C2ES Climate Innovation 2050*; Center for Climate and Energy Solutions: Arlington, VA, USA, 2021.
3. Reynolds, O., IV. On the Theory of Lubrication and Its Application to Mr. Beauchamp Tower's Experiments, Including an Experimental Determination of the Viscosity of Olive Oil. *Philos. Trans. R. Soc. Lond.* **1886**, *177*, 157–234. [CrossRef]

4. Sommerfeld, A. *Zur hydrodynamischen Theorie der Schmiermittelreibung*; Vol. 50, Zeitschrift für Mathematik und Physik; Druck und Verlag von B.G. Teubner: Leipzig, Germany, 1904.
5. Temperly, H.N.V.; Dowson, D.; Godlet, M.; Taylor, C.M. The Tensile Strength of Liquids. In *Cavitation and Related Phenomena in Lubrication*; ASME: New York, NY, USA, 1974; pp. 11–14.
6. Braun, M.; Hannon, W. Cavitation Formation and Modelling for Fluid Film Bearings: A Review. *Proc. Inst. Mech. Eng. Part J J. Eng. Tribol.* **2010**, *224*, 839–863. [CrossRef]
7. Gümbel, L. Das Problem der Lagerreibung. *Mbl. Berlin. Bez. Ver. Dtsch. Ing* **1914**, *5*, 87–104.
8. Cavitation in Lubricating Films. *Tribology* **1968**, *1*, 153–156. [CrossRef]
9. Swift, H.W. The Stability of Lubricating Films in Journal Bearings. *Minutes Proc. Inst. Civ. Eng.* **1932**, *233*, 267–288. [CrossRef]
10. Stieber, W. *Das Schwimmlager: Hydrodynamische Theorie Des Gleitlagers*; VDI-Verlag: Düsseldorf, Germany, 1933.
11. Jakobsson, B.; Floberg, L. *The Finite Journal Bearing, Considering Vaporization: (Das Gleitlager von Endlicher Breite Mit Verdampfung)*; Chalmers Tekniska Högskolas Handlingar: Gothenburg, Sweden, 1957.
12. Olsson, K. *Cavitation in Dynamically Loaded Bearings*; Avd. Maskinteknik; Scandinavian Univ. Books: Oslo, Norway, 1965.
13. Elrod, H.G. A Cavitation Algorithm. *J. Lubr. Technol.* **1981**, *103*, 350–354. [CrossRef]
14. Cole, J.A.; Hughes, C.J. Oil Flow and Film Extent in Complete Journal Bearings. *Proc. Inst. Mech. Eng.* **1956**, *170*, 499–510. [CrossRef]
15. Dowson, D. Investigation of Cavitation in Lubricating Films Supporting Small Loads. In Proceedings of the Proceedings Conference on Lubrication and Wear, London, UK, 1–3 October 1957; Institution of Mechanical Engineers: London, UK, 1957; Volume 93.
16. Smith, E. H. A Study of Film Rupture in Hydrodynamic Lubrication. Ph.D. Thesis, University Leeds, Leeds, UK, 1975.
17. Dowson, D.; Taylor, C.M. Cavitation in Bearings. *Annu. Rev. Fluid Mech.* **1979**, *11*, 35–65. [CrossRef]
18. Swales, P.D.; Dowson, D. A Review of Cavitation Phenomena in Engineering Situations. In *Cavitation and Related Phenomena in Lubrication*; ASME: New York, NY, USA, 1974; pp. 3–9.
19. Dowson, D.; Taylor, C.M. Fundamental Aspects of Cavitation in Bearings. In Proceedings of the 1st Leeds-Lyon Symposium on Tribology, Leeds, UK, September 1974.
20. Jacobson, B.O.; Hamrock, B.J. High-Speed Motion Picture Camera Experiments of Cavitation in Dynamically Loaded Journal Bearings. *Jt. Lubr. Conf.* **1982**, *105*, 446–452. [CrossRef]
21. Jacobson, B.O.; Hamrock, B.J. Vapor Cavitation in Dynamically Loaded Journal Bearings. In Proceedings of the Second International Conference of Cavitation, Edinburgh, UK, 5–8 September 1983.
22. Döring, B.; Hopf, G.; Rudolph, T.; Schüler, D.; Schulte, W. *Große Radiallager - Vorhaben Nr. 293 - Untersuchung der dynamischen Eigenschaften großer Turbinenlager - Abschlussbericht*; FVV | Research Association for Combustion Engines e.V.: Frankfurt am Main, Germany, 1986.
23. Sun, D.C.; Brewe, D.E. A High Speed Photography Study of Cavitation in a Dynamically Loaded Journal Bearing. *ASME J. Tribol.* **1991**, *113*, 287–292. [CrossRef]
24. Shen, C.; Khonsari, M.M. On the Magnitude of Cavitation Pressure of Steady-State Lubrication. *Tribol. Lett.* **2013**, *51*, 153–160. [CrossRef]
25. Yang, H.r.; Wang, X.L.; Zhang, Y.y.; Du, J.f. Study on the Bubbly Lubrication of Journal Bearings at Various Shear Rates and Temperatures. *Tribol. Int.* **2014**, *71*, 132–139. [CrossRef]
26. Poddar, S.; Tandon, N. Detection of Journal Bearing Vapour Cavitation Using Vibration and Acoustic Emission Techniques with the Aid of Oil Film Photography. *Tribol. Int.* **2016**, *103*, 95–101. [CrossRef]
27. Ochiai, M.; Sakai, F.; Hashimoto, H. Reproducibility of Gaseous Phase Area on Journal Bearing Utilizing Multi-Phase Flow CFD Analysis under Flooded and Starved Lubrication Conditions. *Lubricants* **2019**, *7*, 74. [CrossRef]
28. Hagemann, T.; Vetter, D.; Wettmarshausen, S.; Stottrop, M.; Engels, A.; Weißbacher, C.; Bender, B.; Schwarze, H. A Design for High-Speed Journal Bearings with Reduced Pad Size and Improved Efficiency. *Lubricants* **2022**, *10*, 313. [CrossRef]
29. Buchhorn, N.; Stottrop, M.; Bender, B. Influence of Active Cooling at the Trailing Edge on the Thermal Behavior of a Tilting-Pad Journal Bearing. *Lubricants* **2021**, *9*, 26. [CrossRef]
30. Hagemann, T.; Kukla, S.; Schwarze, H. Measurement and Prediction of the Static Operating Conditions of a Large Turbine Tilting-Pad Bearing Under High Circumferential Speeds and Heavy Loads. In Proceedings of the Volume 7B: Structures and Dynamics, San Antonio, TX, USA, 3–7 June 2013; p. V07BT30A019. [CrossRef]
31. Stottrop, M.; Buchhorn, N.; Bender, B. Experimental Investigation of a Large Tilting-Pad Journal Bearing—Comparison of a Flooded and Non-Flooded Design. *Lubricants* **2022**, *10*, 83. [CrossRef]
32. Stottrop, M.; Engels, A.; Weißbacher, C.; Bender, B. Experimental Investigation of a Large Tilting-Pad Journal Bearing With a Direct-Bonded Sub-Millimeter PEEK Lining. In Proceedings of the Volume 11A: Structures and Dynamics—Aerodynamics Excitation and Damping, Bearing and Seal Dynamics, Boston, MA, USA, 26–30 June 2023; p. V11AT22A008. [CrossRef]

33. Reinke, P.; Schmidt, M.; Beckmann, T. Advanced Model Experiment for the Research of Journal Bearings with Cavitation. In Proceedings of the 2019 JSAE/SAE Powertrains, Fuels and Lubricants, Kyoto, Japan, 26–29 August 2019. [CrossRef]
34. Reinke, P.; Ahlrichs, J.; Beckmann, T.; Schmidt, M. Bubble Dynamics in a Narrow Gap Flow under the Influence of Pressure Gradient and Shear Flow. *Fluids* **2020**, *5*, 208. [CrossRef]
35. Reinke, P.; Ahlrichs, J.; Beckmann, T.; Schmidt, M. High-Speed Digital Photography of Gaseous Cavitation in a Narrow Gap Flow. *Fluids* **2022**, *7*, 159. [CrossRef]
36. Reinke, P.; Beckmann, T.; Ahlers, C.; Ahlrichs, J.; Hammou, L.; Schmidt, M. High-Speed Digital Photography of Vapor Cavitation in a Narrow Gap Flow. *Fluids* **2023**, *8*, 44. [CrossRef]
37. Rosenberg, M.D. *Gaseous-Type Cavitation in Liquids*; Acoustics Research Laboratory-Harvard University: Cambridge, MA, USA, 1953.
38. Glienicke, J. Paper 13: Experimental Investigation of the Stiffness and Damping Coefficients of Turbine Bearings and Their Application to Instability Prediction. *Proc. Inst. Mech. Eng. Conf. Proc.* **1966**, *181*, 116–129. [CrossRef]
39. Hopf, G. *Experimentelle Untersuchungen an Großen Radialgleitlagern für Turbomaschinen*; Number 89,5 in Schriftenreihe/Ruhr-Universität Bochum; Fakultät für Maschinenbau, Institut für Konstruktionstechnik, Lehrst. für Maschinenelemente u. Fördertechnik: Bochum, Germany, 1989.
40. Bauer, G. *Ölhydraulik*; Springer Fachmedien Wiesbaden: Wiesbaden, Germany, 2016. [CrossRef]
41. Bruggeman, D.A.G. Berechnung Verschiedener Physikalischer Konstanten von Heterogenen Substanzen. I. Dielektrizitätskonstanten Und Leitfähigkeiten Der Mischkörper Aus Isotropen Substanzen. *Ann. Phys.* **1935**, *416*, 636–664. [CrossRef]

Disclaimer/Publisher's Note: The statements, opinions and data contained in all publications are solely those of the individual author(s) and contributor(s) and not of MDPI and/or the editor(s). MDPI and/or the editor(s) disclaim responsibility for any injury to people or property resulting from any ideas, methods, instructions or products referred to in the content.